Dislocation plasticity effects on interfacial fracture

van der Giessen, E.; Needleman, A.

Published in:
Interface Science

Publication date:
2003

INTERFACE SCIENCE 11, 291–301, 2003

Dislocation Plasticity Effects on Interfacial Fracture

E. VAN DER GIESSEN
University of Groningen, Department of Applied Physics, Nyenborgh 4, 9747 AG Groningen, The Netherlands
Giessen@phys.rug.nl

ALAN NEEDLEMAN
Brown University, Division of Engineering, Providence, RI 02912, USA

Abstract. Analyses are reviewed where plastic flow in the vicinity of an interfacial crack is represented in terms of the nucleation and glide of discrete dislocations. Attention is confined to cracks along a metal-ceramic interface, with the ceramic idealized as being rigid. Both monotonic and fatigue loading are considered. The main focus is on the stress and deformation fields near the crack tip predicted by discrete dislocation plasticity, in comparison with those obtained from conventional continuum plasticity theory. The role that discrete dislocation plasticity can play in interpreting interface fracture properties in the presence of plastic flow is discussed.

Keywords: nucleation of dislocations, metal-ceramic interfaces, cracks, monotonic and fatigue loading, dislocation plasticity

1. Introduction

Metal-ceramic interfaces are found in a variety of components and structures, and fracture at or near such interfaces often limits reliability. Knowledge of the stress and deformation fields at the crack tip at metal-ceramic interfaces is needed in order to develop a fundamental understanding of this fracture process.

The fields in question depend strongly at the length scale at which one observes the crack. An idealized summary of the important length scales involved in the failure of a bi-material interface is shown schematically in Fig. 1. The length scales range from that of the macroscale object to the atomic scale, including the various microstructural length scales in between that are associated with, for example, particles, grains, and defect structures. Many details are left out in this simple picture, but it emphasizes that fracture, i.e. the creation of new surface, is highly localized at the atomic scale, but is driven by the macroscopic applied load communicated to the atomic scale via stress fields on smaller and smaller length scales. It is the precise communication down these scales which determines whether or not crack growth occurs and how much energy is dissipated, e.g. [1]. It should be noted that not all these scales are necesarily present. For instance, in thin metallic films bonded to ceramic substrates, as used in microelectronic devices, the scale of the plastically deforming region may extend over only one or a few crystals.

One issue for interfacial fracture concerns the relation between the bond strength and the remote work and stress applied to a growing interfacial crack. The applied work may have a large contribution from plastic dissipation in the metal, and since the magnitude of this contribution depends on the local fields, it depends on the mode of loading. The bond strength and toughness are the intrinisic interface properties that one would like to extract from a measurement of the work and stress applied during interface crack growth. For example, starting from a small length picture, atomistic calculations of MgO/Ag adhesion give cohesive strengths of 2–10 GPa [2] and values of the work of separation of the order of 0.1–1.0 J/m^2, with the lower values accounting for effects of small concentrations of impurities and segregants. Measured values of interface strength and the applied work of separation cover a wide range

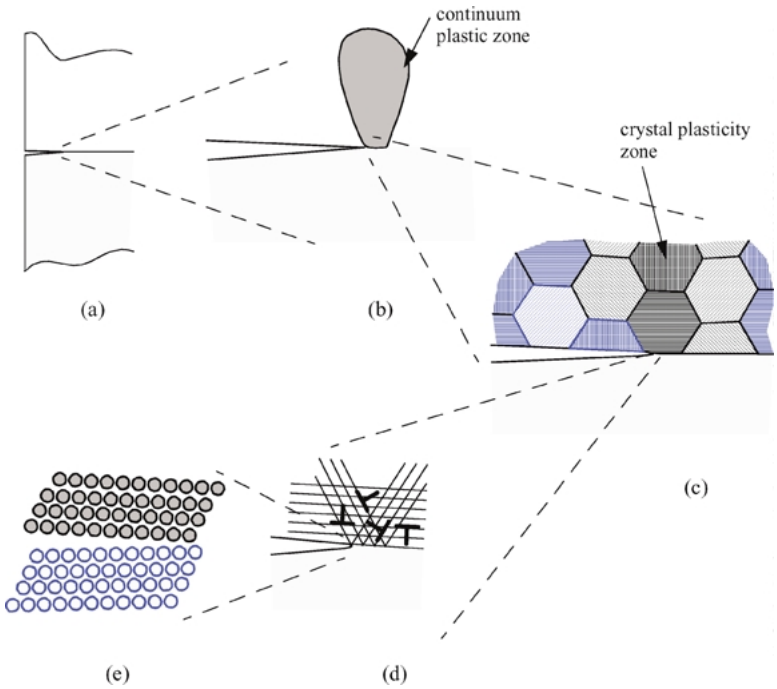

Figure 1. The various relevant scales that may determine the response of a crack along a bi-material interface. (a) Zooming in to the near-tip region, we observe the plastic zone governed by macroscopic continuum plastic flow (b), inside of which we notice that the material is polycrystalline with the plastic deformation being different in different grains (c). Even closer to the tip of the crack, we observe that plastic deformation occurs by the localized slip on particular slip planes caused by the motion of individual dislocations (d). The final illustration (e) shows that the atomic arrangement on either side of the crack.

and are highly system and processing dependent. Typically, measured values of the applied work of separation are 2–5 J/m^2 for interfaces with segregated impurities and sharp cracks, and greater than 200 J/m^2 for clean interfaces with blunt cracks [3]. Gupta and Yuan [4] using a spallation technique report interface strength values of a few hundred MPa and values of the interface work of separation of less than 1 J/m^2. The large difference between atomistically computed values of interfacial fracture strength and energy, and values inferred from the applied work and stress is due to the plastic deformation taking place in the metal near the crack tip. This discrepency is a major issue in estimating cohesive properties from macroscopic observations. For instance, the macroscopically inferred values of the cohesive strength are only several times the flow strength of the metal [3]; much less than the values estimated from atomistics. Thus, there is a significant discrepancy between 'top-down' and 'bottom-up' estimates of the fracture properties.

The role of plastic dissipation in setting the apparent toughness of interface cracks has been investigated by Wei and Hutchinson [5] using a variety of continuum characterizations of plastic flow, including strain gradient plasticity. In the present paper, analyses are discussed that explore the effect of the discrete dislocation structures that form near an interface crack on fracture. According to nonhardening continuum crystal plasticity, the stresses near the crack tip on the continuum scale are not higher than a few times the yield strength of the crystal. Thus, a cohesive surface model with atomistically predicted cohesive strength will not predict any crack growth. However, the discrete dislocation plasticity solutions by Nakatani et al. [6] for interface cracks show that the gradients near the crack tip can induce the development of dislocation structures in which the collective long-range fields of dislocations lead to much increased stress levels. The evolving dislocation structures near an interface crack tip also play an important role in precipitating fatigue, [7].

2. Background: Interfacial Near-Tip Continuum Fields

In order to provide a perspective on the discrete dislocation predictions, some characteristic features of

interface crack tip fields predicted by conventional continuum theories are noted. For a homogeneous elastic solid, the stress state near a crack tip is characterized by a square root singularity. All dependence on geometry and loading is embodied in the stress intensity factor which is the amplitude of this singular field. There are three fracture modes, each with an independent stress intensity factor: mode I involves opening of the crack; mode II involves sliding of the crack faces perpendicular to the crack front; mode III is also a sliding mode, but with the direction of sliding parallel to the crack front. The opening mode, mode I, is of most significance in engineering applications. When all deviations from linear elastic response are confined to a region near the crack tip, i.e. under small-scale yielding conditions, the stress intensity factor characterizes the loading on the nonlinear region and serves as a fracture characterizing parameter. The identification of a crack tip characterizing parameter for interfacial cracks is much less straightforward than for cracks in macroscopically homogeneous solids. For example, the elastic crack-tip fields for a stationary interface crack in a body subject to pure mode I loading have both mode I and mode II components locally. Furthermore, because these fields are oscillatory, the mode mixity, the ratio of the mode I and mode II components, varies with distance from the crack tip. In addition, the near tip fields become compressive and give rise to contact across the bond line. As a consequence, even for linear elastic material behavior, the development of an interfacial fracture mechanics framework is not straightforward [8, 9].

For static plane problems involving isotropic elastic bimaterials, Dundurs [10] observed that isotropic elastic solutions depend on only two non-dimensional combinations of the elastic moduli, namely

$$\begin{aligned}\alpha &= \frac{E_a\left(1-\nu_b^2\right)-E_b\left(1-\nu_a^2\right)}{E_a\left(1-\nu_b^2\right)+E_b\left(1-\nu_a^2\right)},\\ \beta &= \frac{1}{2}\frac{E_a(1-2\nu_b)(1+\nu_b)-E_b(1-2\nu_a)(1+\nu_a)}{E_a\left(1-\nu_b^2\right)+E_b\left(1-\nu_a^2\right)}\end{aligned} \tag{1}$$

where the subscripts a and b refer to the two materials.

For a stationary interface crack, the singular near-tip fields give rise to tractions on $x_2 = 0$ directly ahead of the crack tip that have the form ([8, 11–13]),

$$T_2 + iT_1 = \frac{(K_1 + iK_2)}{\sqrt{2\pi x_1}}(x_1)^{i\epsilon} \quad i = \sqrt{-1} \tag{2}$$

Here, K_1 and K_2 are, respectively, the mode I and mode II stress intensity factors and the oscillatory index ϵ is defined by

$$\epsilon = \frac{1}{2\pi}\ln\frac{1-\beta}{1+\beta} \tag{3}$$

The displacements $u = u_1 + iu_2$ corresponding to the linear elastic singular crack tip field are given by

$$\begin{aligned}u = \frac{2(1+\nu)}{E}&\frac{|K|r^{1/2}}{2\sqrt{2\pi}\cosh(\pi\epsilon)}\\ &\times\left[\frac{(3-4\nu)\exp(\bar\theta - i\bar\psi)-\exp(-\bar\theta - i\bar\psi)}{1-2i\epsilon}\right.\\ &\left.- i\sin\theta\exp(\bar\theta + i\bar\psi)\right]\end{aligned} \tag{4}$$

where

$$r = \sqrt{x_1^2 + x_2^2}, \quad \theta = \tan^{-1}(x_2/x_1), \tag{5}$$

$$\bar\theta = \frac{i\theta}{2} + \epsilon(\theta - \pi), \quad \bar\psi = \psi + \epsilon\ln\left(\frac{r}{L}\right), \tag{6}$$

with

$$\tan\psi = \frac{\Im[KL^{i\epsilon}]}{\Re[KL^{i\epsilon}]} \tag{7}$$

and L a reference length. Here $\Re[\cdot]$ and $\Im[\cdot]$ denote, respectively, the real and imaginary parts of a complex quantity.

The structure of near tip fields for interfacial cracks in isotropic elastic-plastic solids was elucidated by Shih, Asaro and co-workers in a series of papers, see e.g. [14–16]. At a smaller scale, where the discreteness of slip systems comes into play and the plastic response is anisotropic, analytical solutions for near tip fields in single crystals have been presented in [6]. These solutions pertain to plane strain small-scale yielding conditions for a nonhardening single crystal bonded to a rigid substrate. The method of solution follows that in [17] and [18]. Solutions were obtained for two slip system and three-slip system fcc-type and bcc-type crystal geometries. The fcc-type crystal has slip systems at angles of $\phi^{(\alpha)} = (54.7^\circ, 125.3^\circ, 0^\circ)$ to the crack line, while the three slip systems for the bcc-type crystal are oriented at $\phi^{(\alpha)} = 35.3^\circ, 144.7^\circ, 90^\circ)$. As for homogeneous crystals [17], the character of the solutions is that the stress is constant in sectors.

Figures 2 and 3 illustrate solutions for the three slip system fcc type and bcc type crystal geometries, respectively. Each figure shows (a) the interface crack

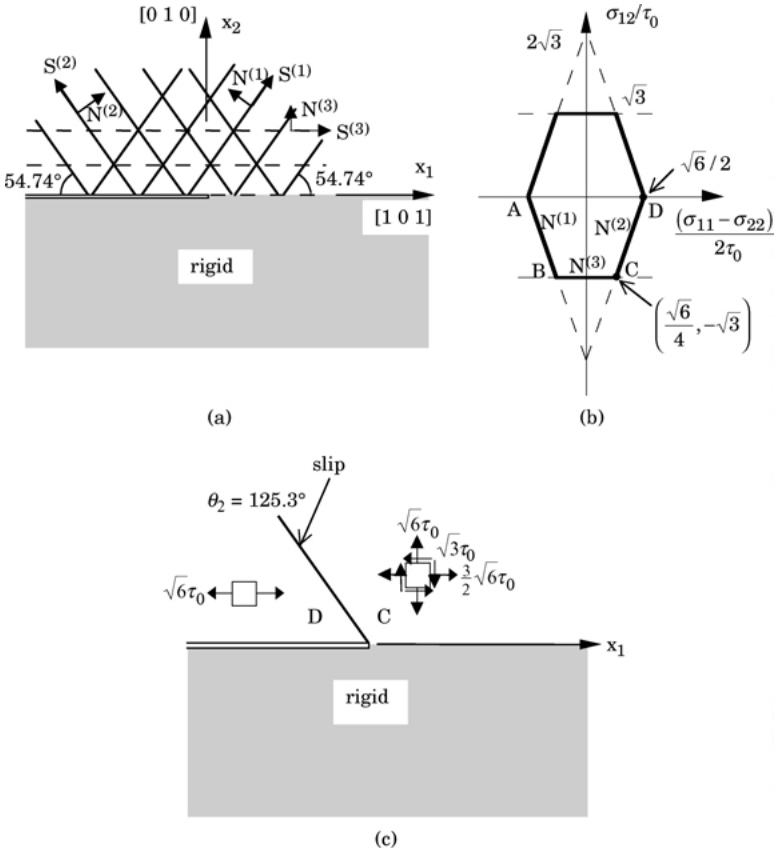

Figure 2. Interface crack between a three-slip system fcc type crystal and a rigid substrate: (a) physical plane illustrating slip plane traces; (b) stress plane showing the yield surface; (c) asymptotic analytical solution in agreement with the discrete dislocation simulations. From [6].

configuration, (b) the single crystal yield surface and (c) the sector geometry. The stress states in (c) denoted by C and D correspond to the yield surface vertices C and D in (b). The solutions for a nonhardening crystal are not unique and the solutions shown in Figs. 2 and 3 were chosen to match the discrete dislocation plasticity solutions to be discussed in Section 4.

For the fcc crystal geometry, the stress state in the two sectors is given by

$$\text{Sector C:}\quad \frac{\sigma_{11}-\sigma_{22}}{2\tau_0}=\frac{\sqrt{6}}{4},\quad \frac{\sigma_{11}+\sigma_{22}}{2\tau_0}=\frac{5\sqrt{6}}{4},\quad \frac{\sigma_{12}}{2\tau_0}=-\sqrt{3} \tag{8}$$

$$\text{Sector D:}\quad \frac{\sigma_{11}-\sigma_{22}}{2\tau_0}=\frac{\sqrt{6}}{2},\quad \frac{\sigma_{11}+\sigma_{22}}{2\tau_0}=\frac{\sqrt{6}}{2},\quad \frac{\sigma_{12}}{2\tau_0}=0 \tag{9}$$

The two sectors are separated by a slip band (the slip direction is along the band).

For the bcc type crystal geometry, the stress state in the two sectors is

$$\text{Sector C:}\quad \frac{\sigma_{11}-\sigma_{22}}{2\tau_0}=\frac{3\sqrt{2}-\sqrt{6}}{4},\quad \frac{\sigma_{11}+\sigma_{22}}{2\tau_0}=\frac{3}{4}(\sqrt{6}+\sqrt{2}),\quad \frac{\sigma_{12}}{2\tau_0}=-\sqrt{3} \tag{10}$$

$$\text{Sector D:}\quad \frac{\sigma_{11}-\sigma_{22}}{2\tau_0}=\frac{3\sqrt{2}}{4},\quad \frac{\sigma_{11}+\sigma_{22}}{2\tau_0}=\frac{3\sqrt{2}}{4},\quad \frac{\sigma_{12}}{2\tau_0}=0 \tag{11}$$

and the band separating them is a kink band (the slip direction is perpendicular to the band).

These simple solutions are exact asymptotic solutions under the assumed conditions and give insight

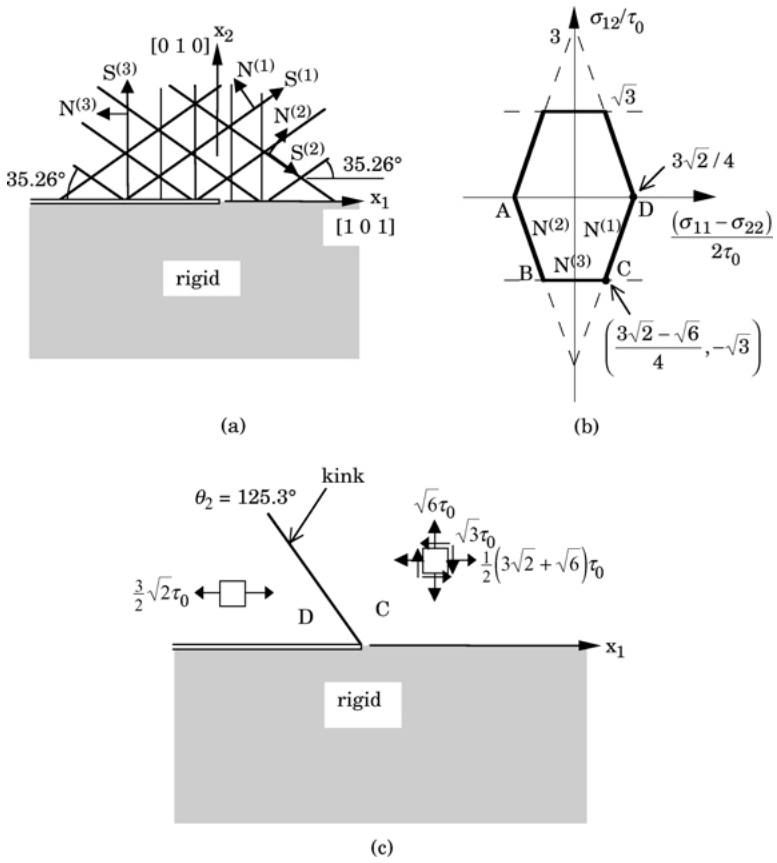

Figure 3. Interface crack between a three-slip system bcc type crystal and a rigid substrate: (a) physical plane illustrating slip plane traces; (b) stress plane showing the yield surface; (c) asymptotic analytical solution in agreement with the discrete dislocation simulations. From [6].

into the nature of the near crack tip fields. For both the fcc and bcc type crystal geometries, the opening stress, σ_{22} is maximum in Sector C (it vanishes in Sector D) and has the value $\sqrt{6}\tau_0 \approx 2.45\tau_0$. Opening stress levels of a few times the flow strength are a characteristic feature of nonhardening continumm plasticity crack tip fields. Finite element analyses of crack tip fields for nonhardening (but slightly rate dependent, for numerical convenience) fcc and bcc type crystals were also carried out in [6]. Since the finite element solutions are full field solutions, they provide an indication of the range of validity of the asymptotic results. The structure of the crack tip fields from the finite element analyses was found to be in good agreement with the analytical predictions.

3. Discrete Dislocation Model

The role of discrete dislocations near the tip of a crack emerges in the model problem that was initiated within a discrete dislocation dynamics framework by Cleveringa et al. [19], and is illustrated in Fig. 4. A plane strain, small-scale yielding problem under mode I remote loading was analyzed with discrete dislocations confined to a region surrounding the initial crack tip. By making use of symmetry, only half of the problem needed to be analyzed in [19] with the transgranular crack on the symmetry plane and appropriate boundary conditions, i.e. $T_1 = u_2 = 0$ along $x_2 = 0$. Nakatani et al. [6] analyzed a similar problem, but confined attention to stationary cracks, and took the $x_2 = 0$ crack plane to be the bond line with a rigid substrate (see Section 4). Fatigue crack growth along a single crystal-rigid substrate interface was analyzed by Deshpande et al. [7] (see Section 5).

Crack propagation, when it occurs, is taken into account through the use of a cohesive surface laid out in front of the crack tip. The properties of this cohesive surface are prescribed in the form given by Xu and Needleman [20] which allows for shear as well as

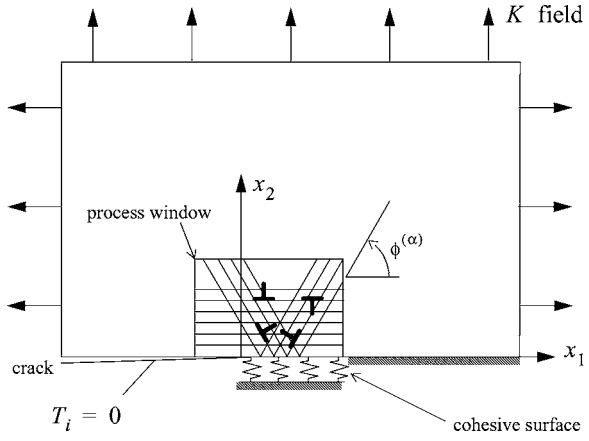

Figure 4. Small-scale yielding analysis for a plastically deforming solid. The model can be used for a symmetric mode I crack problem and for an interfacial crack, depending on the boundary conditions along $x_2 = 0$.

opening decohesion and is based on the universal binding law [21]. The normal and tangential tractions are thus given by

$$T_i = -\frac{\partial \varphi}{\partial \Delta_i}, (i = n, t) \tag{12}$$

with

$$\varphi = \varphi_n + \varphi_n \exp\left(-\frac{\Delta_n}{\delta_n}\right)\left\{\left[1 + \frac{\Delta_n}{\delta_n}\right](q-1) - q\left[1 + \frac{\Delta_n}{\delta_n}\right]\exp\left(-\frac{\Delta_t^2}{\delta_t^2}\right)\right\}. \tag{13}$$

Here, φ_n is the normal work of separation and φ_t is the shear work of separation, which can be expressed as

$$\varphi_n = e\sigma_{\max}\delta_n, \quad \varphi_t = \sqrt{\frac{e}{2}}\tau_{\max}\delta_t \tag{14}$$

in terms of the normal strength $\sigma_{\max}$ and tangential strength $\tau_{\max}$, and the characteristic lengths δ_n and δ_t ($e = \exp(1)$). The coupling between normal and tangential separation is governed by $q = \varphi_t/\varphi_n$ (and the parameter r in [20] is taken to be zero). The work of separation can be related to a reference stress intensity factor K_0 by the small scale yielding relation

$$K_0 = \sqrt{\frac{E\varphi_n}{1-\nu^2}}. \tag{15}$$

The significance of K_0 is that pure mode I crack growth in a homogeneous elastic solid with the given cohesive properties takes place at $K_I/K_0 = 1$. The quantity K_0 is a measure of the energy per unit area required to create new free surface; the fracture strength under monotonic loading conditions, K_{Ic}, will usually be significantly greater than K_0 due to plastic dissipation by dislocation motion.

All dislocations were assumed to be of edge character and to live on slip planes oriented at $\phi^{(\alpha)}$, $\alpha = 1, 2, 3$. They were treated as line singularities in an elastic (isotropic) metal. The long-range interactions between the dislocations as well as their interactions with the crack and the interface is accounted for through their elastic fields. These fields are the solution of the boundary value problem in Fig. 4, which is obtained by making use of the decomposition proposed originally in [22]. In the presence of a cohesive surface ahead of the crack tip, the problem is nonlinear and an incremental approach is needed, where the velocity, strain-rate and stress-rate fields are written as the superposition of two fields,

$$\dot{u}_i = \tilde{\dot{u}}_i + \hat{\dot{u}}_i, \quad \dot{\epsilon}_{ij} = \tilde{\dot{\epsilon}}_{ij} + \hat{\dot{\epsilon}}_{ij}, \quad \dot{\sigma}_{ij} = \tilde{\dot{\sigma}}_{ij} + \hat{\dot{\sigma}}_{ij}. \tag{16}$$

The $\tilde{(\ )}$ fields are the singular fields of the individual dislocations, in their current configuration, and give rise to tractions $\tilde{T}_i$ and displacements $\tilde{U}_i$ on the boundary of the body. In [19], the fields in an infinite half spase were used, while the fields for infinite space were employed in [6]. The $\hat{(\ )}$ fields represent the image fields that correct for the actual boundary conditions. Using a finite element method, they are computed in an incremental fashion after each incremental change in the dislocation configuration, taking due care of the opening displacement increments on the cohesive surface during the time step (see [19] for details).

With the decomposition (16), the Peach-Koehler force $f^{(I)}$ on the Ith dislocation is given by

$$f^{(I)} = n_i^{(I)}\left(\hat{\sigma}_{ij} + \sum_{J \neq I}\sigma_{ij}^{(J)} + \Sigma_{ij}^{(I)}\right)b_j^{(I)}. \tag{17}$$

with $n_i^{(I)}$ the slip plane normal, $b_j^{(I)}$ the Burgers vector and $\Sigma_{ij}^{(I)}$ the image field on dislocation I due to the traction-free surface.[1] The Peach-Koehler force includes the long-range interactions with all other dislocations in the material. In any point not coinciding with a dislocation, the Peach-Koehler force can be computed from Eq. (17) by summation over all J and

with $\Sigma_{ij} = 0$; its value is then equal to the resolved shear stress times the magnitude of the Burgers vector, b. It is this force that will determine the evolution of the dislocation structure, accounting for glide, generation, annihilation and pinning at obstacles. These mechanisms are controlled by physical processes on the atomic scale, which are not resolved in discrete dislocation plasticity and which are therefore incorporated through a set of constitutive rules [23]. Dislocation glide is assumed to be governed by a linear drag relation between the dislocation velocity and the Peach-Koehler force. Dislocations can be generated from Frank-Read sources which are modeled in two dimensions as point sources that generate a dislocation dipole when the Peach-Koehler force exceeds a critical value of $\tau_{\text{nuc}}b$ during a period of time t_{nuc}. Obstacles, which could be small precipitates or forest dislocations, pin dislocations and will release them once the Peach-Koehler force attains the obstacle strength $\tau_{\text{obs}}b$. Annihilation of two dislocations with opposite Burgers vector occurs when they approach each other within a critical annihilation distance L_e. In the results to be discussed subsequently, sources and obstacles were static entities and randomly distributed in the process window of Fig. 4(a).

4. Cracks under Monotonic Loading

Nakatani et al. [6] carried out an analysis of the type discussed above for a stationary crack along an interface between a single crystal and a rigid substrate. A stiff cohesive surface was specified along $x_2 = 0$, giving an approximately perfect bond. No mobile dislocations are present initially. An initial distribution of dislocation sources and obstacles is specified in a process window about the crack tip. Displacements of the form (4) are prescribed on the remote boundary with $K_2 = 0$ and K_1 the prescribed monotonically increasing parameter.

Slip contours for two of the slip system geometries considered by Nakatani et al. [6] are shown in Figs. 5 and 6. These correspond, respectively, to the fcc-type and bcc-type crystal geometries for which the analytical solutions are sketched in Figs. 2 and 3. For each slip system, the amount of slip, denoted by α, is defined as the accumulated signed Burgers vector, with the sign convention defined in the insets of each figure.

In Fig. 5, for the three-slip system fcc type crystal geometry, the slip band on the $\phi^{(2)} = 125.3^\circ$ slip system behind the crack tip gives rise to an intense band of deformation. The main activity on the $\phi^{(1)} = 54.7^\circ$ slip system is in a kink type band essentially coinciding with the slip band. The abrupt change in sign of the slip on the $\phi^{(3)} = 0^\circ$ slip system across the shear band is seen in Fig. 5(c). Ahead of the crack tip there is considerable activity on the $\phi^{(3)} = 0^\circ$ slip system.

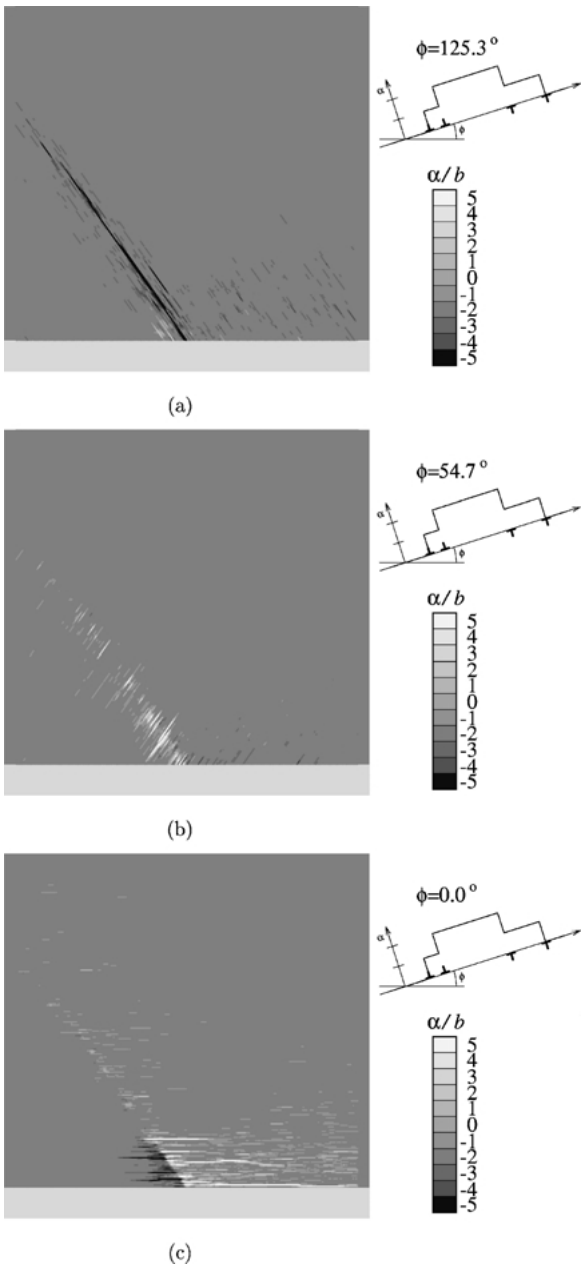

Figure 5. Slip distribution for the three-slip system fcc type crystal geometry at $K_1/K_0 = 0.717$. The size of the region shown is 24 × 24 μm. (a) $\phi^{(2)} = 125.3^\circ$. (b) $\phi^{(1)} = 54.7^\circ$. (c) $\phi^{(3)} = 0^\circ$. From [6].

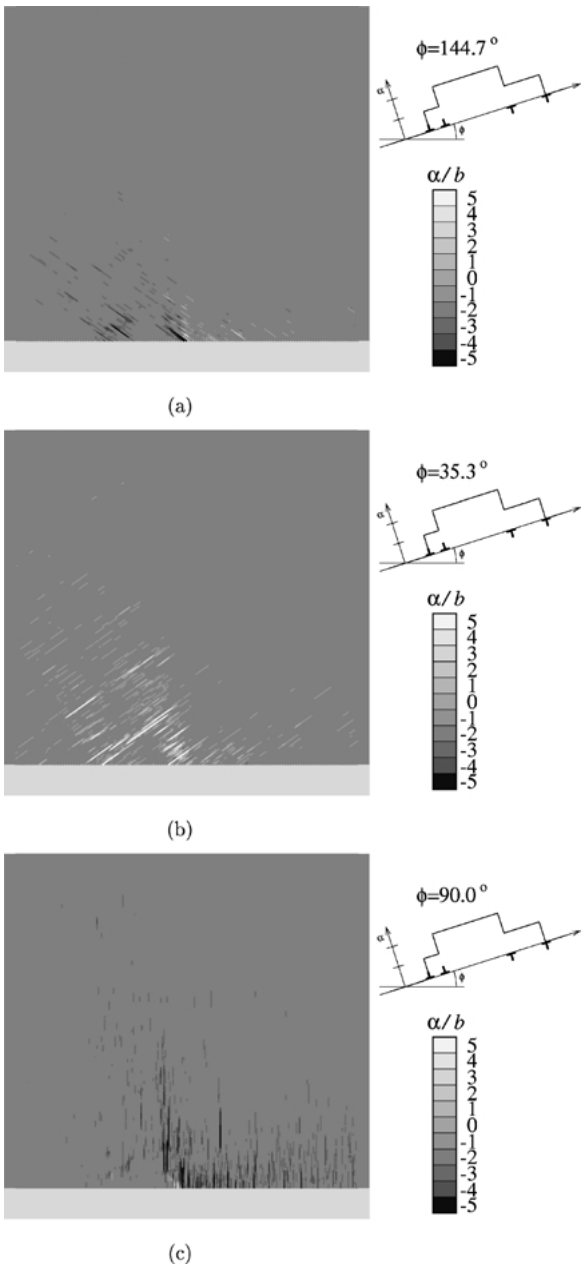

Figure 6. As Fig. 5 but for the bcc type crystal geometry. (a) $\phi^{(2)} = 144.7^\circ$. (b) $\phi^{(1)} = 35.3^\circ$. (c) $\phi^{(3)} = 90^\circ$. From [6].

For the three-slip system bcc type crystal geometry, Fig. 6, are consistent with intense deformation bands along the 35.3° and 144.7° slip systems. There is also slip behind the crack tip in Fig. 6b involving kink type slip for the $\phi^{(1)} = 35.3^\circ$ slip system. There is also slip activity on the 90° slip system, ahead of the crack tip and directly above it.

The most intense deformation for the fcc type crystal geometry is a slip band on the $\phi^{(2)} = 125.3^\circ$ system, while for the bcc type crystal geometry the deformation is most intense in a kink mode behind the crack tip. This has an overall consistency with the analytical and finite element solutions for nonhardening crystals in [6]. Indeed, since the continuum nonhardening crystal solutions are nonunique, one basis for choosing the analytical solutions in Figs. 5 and 6 was because of their similarity to the discrete dislocation deformation modes. Nevertheless, there is a significant difference between the continuum slip predictions and the discrete dislocation predictions; in the discrete dislocation analyses, the opening stress very near the crack tip is substantially higher than predicted by continuum slip plasticity. Although crack growth calculations were not carried out in [6], the dual role played by discrete dislocations in the crack tip vicinity was evident: the dissipation associated with dislocation motion is what leads to a toughness much higher than that associated with the work of creating new surface, while the local stress concentration associated with near tip dislocation patterning induces stress levels much higher than predicted by conventional continuum plasticity, which can eventually precipitate fracture, cf. [19].

5. Fatigue Crack Growth

The dual role of dislocations emerges also under cyclic loading. A series of calculations by Deshpande et al. [7, 24, 25] with essentially the same model but subject to saw-tooth cycling of K between $K_{\max}$ and $K_{\min}$, revealed (i) threshold behavior, (ii) followed by a Paris-like growth regime, as well as (iii) anomalous behavior for short cracks. These phenomena are the outcome of the simulations as a consequence of the irreversibility of plastic flow and of the cohesive surface. Irreversibility of plastic flow is due to the fact that during a loading-unloading sequence, the dislocations do not move back to their initial positions, partly because of their long-range interactions.

For a crack along a perfectly bonded interface, the near-tip fields are inherently mixed mode involving both mode I (tension) and mode II (shear), even for remote tensile loading, with the mode I to mode II ratio varying with distance from the crack tip, e.g. [9] or Eqs. (2)–(7). On the other hand, if the shear cohesive stiffness of the interface is zero, the much simpler homogeneous mode I linear elastic crack tip fields prevail. Neither of these is an exact solution for the

relatively weak interfaces considered. The displacement boundary conditions corresponding to the homogeneous mode I linear elastic crack tip fields have the advantage, for the rectangular region analyzed, that the reference length appearing in (7) needs not be specified. Even though the homogeneous mode I field is prescribed on the remote boundary, the stiffness mismatch between the crystal and the substrate gives rise to mixed mode loading conditions within the process zone.

For an interface crack, Deshpande et al. [7] take the values of the opening and shear cohesive strengths in (14) to be $\sigma_{\max} = 0.3$ GPa and $\tau_{\max} = 0.699$ GPa, respectively, the corresponding values of the work of separation are $\varphi_n = \varphi_t = 0.408$ J/m^2. These values of the interface cohesive strength are consistent with experimental measurements in [4], and for comparison purposes, we note that a representative value of the plane strain tensile flow strength is 50–60 MPa, [25].

Irreversibility in opening the crack may result from oxidiation and is modeled by a modification of the cohesive relation in [20] as sketched in Fig. 7. The irreversibility is only specified for the normal tractions in the irreversible cohesive law and aims at simulating surface contact due to the formation of oxide layers on the newly formed surfaces. The relations (12)–(14) describe the loading response as the traction increases from A up to the maximum value at B, followed by softening while the formed crack opens further. Unloading from any point C takes place along path CD. Upon reloading the traction increases along DC and then follows the original softening curve BCE. The irreversible cohesive relation neglects any irreversibility

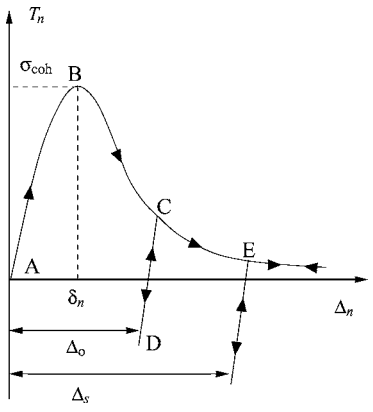

Figure 7. Irreversible cohesive behavior used in the fatigue calculations. The remnant opening Δ_o mimics the effect of an oxide layer formed during opening beyond δ_n.

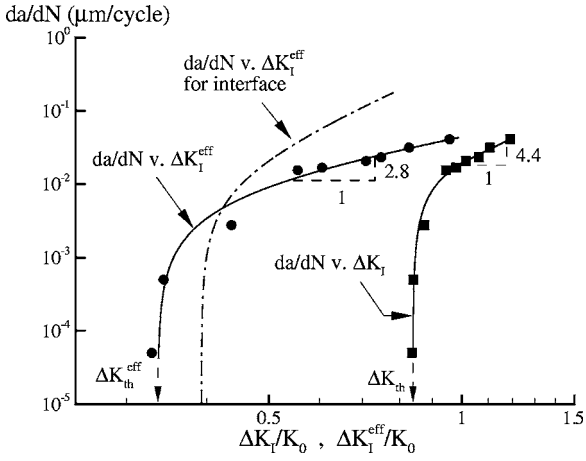

Figure 8. The cyclic crack growth rate da/dN versus $\Delta K_I/K_0$ and $\Delta K_I^{\text{eff}}/K_0$ for the mode I cyclic loading of the single crystal ($R = 0.3$). The slopes of the curves marked correspond to the Paris law exponents for the curves fitted through the numerical results. From [7].

in the tangential tractions. Also, the permanent opening is not permitted to exceed a specified value Δ_s that is specified to be 4 nm.

A summary of the results obtained in [7] for $R = K_{\min}/K_{\max} = 0.3$ is shown in Fig. 8. The figure shows results for both an interface crack and for a (transgranular) crack in a symmetric crystal under mode I conditions. In both cases, surface contact takes place in the wake of the crack due to the formation of oxide layers on the newly created surfaces. This strongly affects the behavior with the irreversible cohesive law in Fig. 7. When the crack faces are in contact, the stresses in the vicinity of the crack tip are much reduced, inhibiting dislocation nucleation and glide as well as lessening the driving force for separation. As a consequence, crack propagation takes place only during the fraction of the fatigue loading cycle in which the crack faces at the tip are separated. The effective stress intensity range ΔK^{eff} responsible for crack growth is

$$\Delta K_{\text{I}}^{\text{eff}} = \begin{cases} K_{\max} - K_{\text{op}} & \text{for } K_{\min} < K_{\text{op}} \\ \Delta K_{\text{I}} & \text{for } K_{\min} \geq K_{\text{op}} \end{cases} \tag{18}$$

This quantity is plotted in Fig. 8 along with the base intensity range ΔK_{I}. The results reveal a threshold in applied $\Delta K_{\text{I}}^{\text{eff}}$ below which there is no crack growth, while above the threshold the response approaches a Paris-like power law $da/dN \propto (\Delta K_{\text{I}}^{\text{eff}})^m$. For the interface crack, the exponent $m \approx 5$ is somewhat higher than for the transgranular crack. The effect of the mode

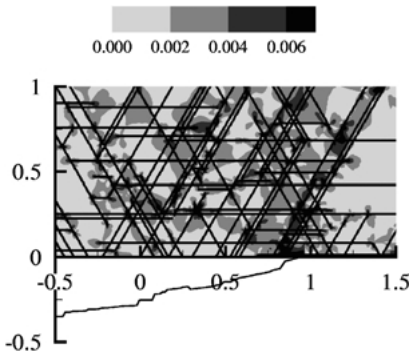

Figure 9. Contours of the slip measure Γ showing discrete slip traces at intervals of $\approx$0.15 μm on 60° slip planes in the wake of a propagating fatigue crack. All distances are in μm. The crack opening profile (displacements magnified by a factor of 20) is plotted below the x_1-axis. From [7].

mixity at the interface is to increase the fatigue threshold of the interface crack but to reduce its resistance to cyclic crack growth at higher values of ΔK_{I}. This behavior is expected to be dependent on the degree of mode mixity and hence affected by the cohesive properties and by the applied loading.

Figure 9 shows distributions in the near-tip region of Γ, which provides an approximate measure of the amount of slip [7]. The slip pattern is very similar to that seen in the experimental investigations in [26, 27] for cyclic crack advance at Al–Al_2O_3 interfaces. Also, consistent with experimental observations, the slip band spacing in Fig. 9 is greater than the crack growth rate, da/dN, by a factor of approximately 2.7. Slip traces in the wake of the propagating fatigue crack are often cited as evidence for a deformation controlled alternating slip mechanism of fatigue crack propagation, e.g. [28, 29]. However, such slip traces also occur near interface cracks and the kinematics of crack growth along an interface by a duplex slip type mechanism is unclear. The calculations in Deshpande et al. [7] describe separation in terms of a cohesive separation model, which is both stress and deformation controlled. More or less uniformly spaced slip traces are an outcome of the analysis.

6. Concluding Remarks

Analyses of interface cracks along metal-ceramic interfaces have been discussed where plastic flow arises from the collective motion of large numbers of discrete dislocations. In the crack growth analyses, a cohesive surface was used to characterize the interface fracture properties.

- For stationary cracks, the overall structure of the crack tip fields is consistent with solutions based on conventional continuum crystal plasticity. However, the gradients near the crack tip induce the development of dislocation structures in which the collective long-range fields of dislocations lead to stress levels much higher than predicted by conventional continuum plasticity.
- The high stress levels that are a consequence of the near-tip discrete dislocation structures precipitate fracture both under monotonic and cyclic loading conditions.
- The stress enhancement from discrete dislocation structures can also affect crack nucleation. For example, in thin films on silicon substrates dislocations pile up against the interface as thin film cools from the processing temperature, [30]. This leads to size effects seen in experiments, but in addition the resulting stress concentration may induce the initiation of delamination.
- The values of the cohesive strength used in the discrete dislocation crack growth calculations were still smaller than the cohesive strengths predicted by atomistic calculations, e.g. [21, 31, 32], which are typically 10–15 GPa. Recent calculations by van der Ven and Ceder [33] indicate the possibility that impurities can drastically reduce this high cohesive strength. Such impurity effects are likely to be particularly important for interfacial fracture.
- Under cyclic loading conditions, interface crack growth can occur when the driving force is less than what is needed for the crack to grow under monotonic loading conditions. Both a threshold and Paris-law type regimes are outcomes of discrete dislocation plasticity calculations, with plastic dissipation playing a key role in the transition.
- Striations emerge as traces of concentrated slip on the newly created free metal surface for cracks propagating along metal-ceramic interfaces.

Acknowledgments

Support from the AFOSR MURI at Brown University on *Virtual Testing and Design of Materials: A Multiscale Approach* (AFOSR Grant F49620-99-1-0272) is gratefully acknowledged. E. van der Giessen also acknowledges support from the Netherlands

Institute of Metals Research and from the Foundation for Fundamental Research of Matter (FOM) in the Netherlands within their research program on *Microstructure Evolution in Materials*.

Note

1. This contribution was omitted in [19], but included in subsequent analyses.

References

1. J.W. Hutchinson and A.G. Evans, Acta Mat. **48**, 125 (2000).
2. T. Hong, J.R. Smith, and D.J. Srolovitz, Acta Metall. Mater. **43**, 2721 (1995).
3. A.G. Evans, J.W. Hutchinson, and Y. Wei, Acta Mater. **47**, 4093 (1999).
4. V. Gupta and J. Yuan, J. Appl. Phys. **74**, 2397 (1993).
5. Y. Wei and J.W. Hutchinson, Int. J. Frac. **95**, 1 (1999).
6. A. Nakatani, W.J. Drugan, E. van der Giessen, and A. Needleman, Crack Tip Fields at a Ductile Single Crystal-Rigid Material Interface, Int. J. Frac. (in print).
7. V.S. Deshpande, A. Needleman, and E. van der Giessen, Acta Materialia **50**, 831 (2002).
8. J.R. Rice, J. Appl. Mech. **55**, 98 (1988).
9. J.W. Hutchinson and Z. Suo, Adv. Appl. Mech. **29**, 69 (1992).
10. J. Dundurs, J. Appl. Mech. **36**, 650 (1969).
11. A.H. England, J. Appl. Mech. **32**, 400 (1965).
12. F. Erdogan, J. Appl. Mech. **32**, 403 (1965).
13. J.R. Rice and G.C. Sih, J. Appl. Mech. **32**, 418 (1965).
14. C.F. Shih and R.J. Asaro, J. Appl. Mech. **55**, 299 (1988).
15. C.F. Shih, R.J. Asaro, and N.P. O'Dowd, J. Appl. Mech. **58**, 450 (1991).
16. C.F. Shih, Mat. Sci. Engin. **A143**, 77 (1991).
17. J.R. Rice, Mech. Mat. **6**, 317 (1987).
18. W.J. Drugan, J. Mech. Phys. Solids **49**, 2155 (2001).
19. H.H.M. Cleveringa, E. van der Giessen, and A. Needleman, J. Mech. Phys. Solids **48**, 1133 (2000).
20. X.-P. Xu and A. Needleman, Model. Simul. Mat. Sci. Engrg. **1**, 111 (1993).
21. J.H. Rose, J. Ferrante, and J.R. Smith, Phys. Rev. Lett. **47**, 675 (1981).
22. E. van der Giessen and A. Needleman, Model. Simul. Mat. Sci. Engrg. **3**, 689 (1995).
23. L.P. Kubin, G. Canova, M. Condat, B. Devincre, V. Pontikis, and Y. Bréchet, Solid State Phenomena **23/24**, 455 (1992).
24. V.S. Deshpande, A. Needleman, and E. van der Giessen, Acta Mat. **49**, 3189 (2001).
25. V.S. Deshpande, A. Needleman, and E. van der Giessen, Acta Mat. **51**, 1 (2003).
26. J.M. McNaney, R.M. Cannon, and R.O. Ritchie, Acta Mat. **44**, 4713 (1996).
27. P. Peralta, U. Ramamurty, S. Suresh, G.H. Campbell, W.E. King, and T.E. Mitchell, Phil. Mag. **A80**, 2109 (2000).
28. C. Laird and G.C. Smith, Phil. Mag. **7**, 847 (1962).
29. P. Neumann, Acta Metall. **17**, 1219 (1969).
30. L. Nicola, E. van der Giessen, and A. Needleman, J. Appl. Phys. **93**, 5920 (2003).
31. G. Lu, D. Orlikowski, I. Park, P. Politano, and E. Kaxiras, Phys. Rev. B **65**, 064102 (2002).
32. E.A.A. Jarvis, R.L. Hayes, and E.A. Carter, Chem. Phys. Chem. **1**, 55 (2001).
33. A. van der Ven and G. Ceder, Phys. Rev. B rapid commun. **67**, 060101 (2003).